Science Advances

▶AAAS

Supplementary Materials for

In situ manipulation and switching of dislocations in bilayer graphene

Peter Schweizer, Christian Dolle, Erdmann Spiecker*

*Corresponding author. Email: erdmann.spiecker@fau.de

The PDF file includes:

Fig. S1. Stacking orders in bilayer graphene.
Fig. S2. Imaging modes in tSEM.
Fig. S3. Manipulation of a dislocation without mechanical cleaning.
Fig. S4. The relationship between dislocation type and line width.
Fig. S5. Example demonstrating the interplay of membrane topography and dislocation line direction.
Fig. S6. AA stacking in dislocation nodes.
Fig. S7. Complete analysis of the Burgers vector of dislocations.
Fig. S8. Dislocation interaction with free edges.
Legends for movies S1 to S4

Other Supplementary Material for this manuscript includes the following:

(available at advances.sciencemag.org/cgi/content/full/4/8/eaat4712/DC1)

Movie S1 (.mp4 format). Exemplary cleaning of bilayer graphene.
Movie S2 (.mp4 format). Manipulation of three individual dislocations showing fundamental properties of dislocations.
Movie S3 (.mp4 format). Manipulation of an array of dislocations pinned to threading dislocations.
Movie S4 (.mp4 format). The whole, unabridged manipulation from movie S3.
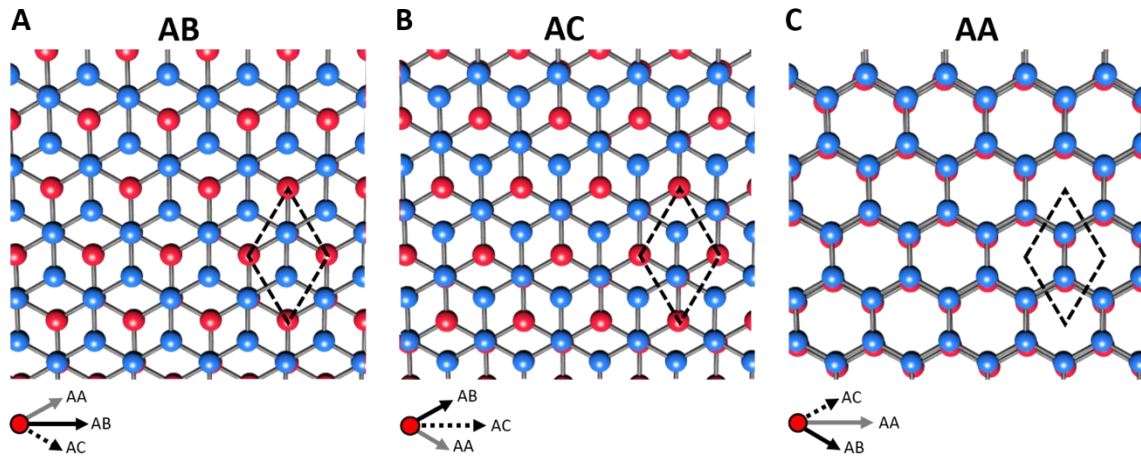
Supplementary Figures

Fig. S1. Stacking orders in bilayer graphene. Schematic of **A** AB-. **B** AC- and **C** energetically unfavored AA-stacking of bilayer graphene. The rhombus signifies the unit cell. All stacking orders can be transferred to any other stacking order by a shift of the lattice of the lower layer as shown below the images. These lattice shifts are realized by introduction of in-plane dislocations as linear topological defects. The Burgers vector of the dislocation corresponds to the lattice shift. For perfect dislocations the Burgers vector equals a lattice translation vector and there is no change in stacking order across the dislocation (e.g. AB → AB). In contrast, for partial dislocations the Burgers vector is shorter than a lattice translation vector resulting in a change in stacking order (e.g., AB → AC). The Burgers vector of a partial dislocation is of type $\frac{a}{3}\langle 1\bar{1}00\rangle$ and has a length of $|\vec{b}| = 1.42$ Å. Due to the absence of stacking fault energy (AB and AC are energetically equivalent), only partial dislocations are found in bilayer graphene *(10)*. If three partial dislocations with all three possible Burgers vectors meet in a single point energetically unfavorable AA-stacking occurs in the center of the node *(26)*.
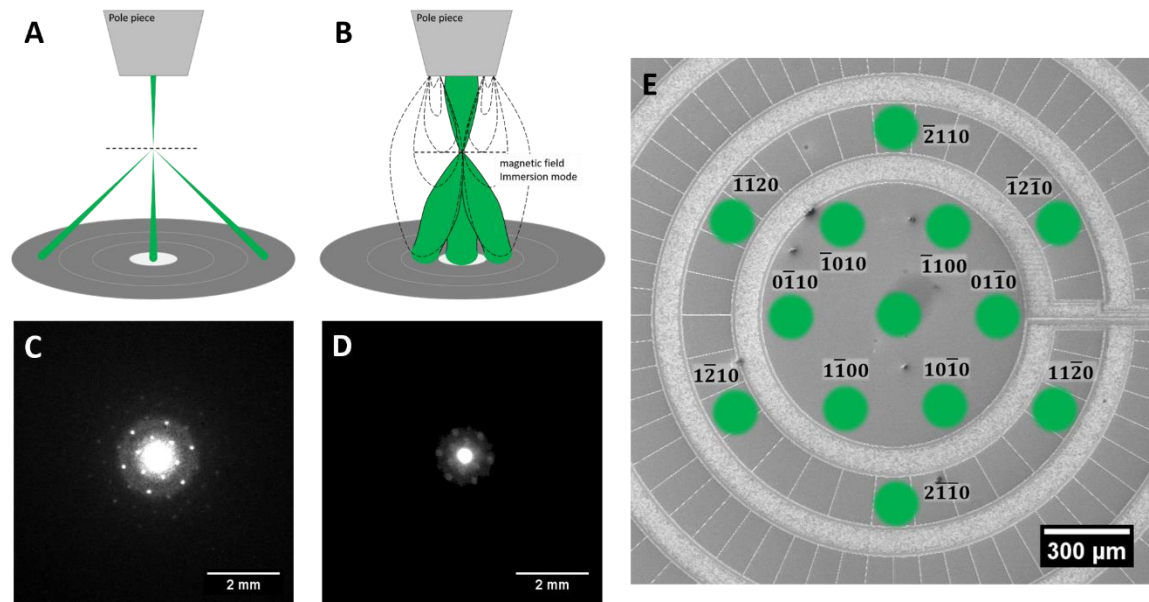
Fig. S2. Imaging modes in tSEM. A Schematic beam trajectory for field-free tSEM imaging mode. The electron beam is diffracted at the crystalline lattice planes and propagates linearly towards the STEM III detector. **B** Schematic beam trajectory for immersion mode. A magnetic field protruding from the pole piece changes the linear trajectory of the electrons (above and below the sample) effectively increasing the convergence angle (on the sample) and reducing the size of the diffraction pattern (on the STEM detector). **C** and **D** show experimental diffraction patterns (taken with imaging plates placed below the sample) of bilayer graphene in field-free mode (**C**) and immersion mode (**D**) at a working distance of 4.2 mm and a primary electron energy of 20 keV. **E** STEM III detector setup for tSEM experiments. Electrons scattered at $\{11\bar{2}0\}$ planes are collected in DF1 enabling visualization of dislocations in bilayer graphene with pronounced contrast (similar to $\{11\bar{2}0\}$ DF-TEM data).
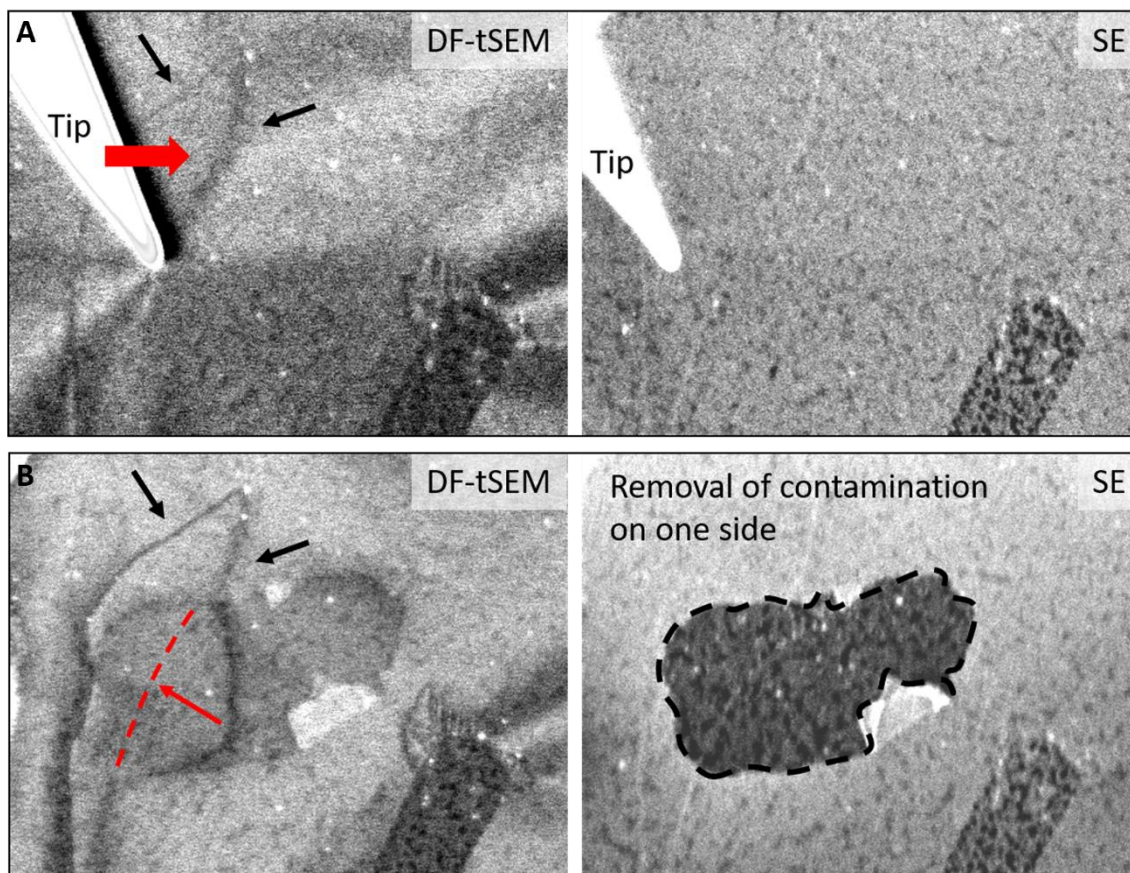
Fig. S3. Manipulation of a dislocation without mechanical cleaning. A The initial
state as shown by DF-tSEM and secondary electron (SE) imaging. Two dislocations are
visible in the tSEM image (marked by black arrows) although the image quality suffers
greatly from contamination. The SE image shows a continuous layer of contaminants on
the graphene surface. The manipulator moves to the right (as indicated by the red arrow)
to change the configuration of one dislocation, leaving it in the state seen in **B**. The
increase in dislocation line length also increases the total defect energy. The expected
energy minimization by line shortening (as indicated by the dashed red line) is not
occurring which implies, that the dislocation movement is inhibited without an external
stimulus. This can be attributed to the contamination still remaining on one of the
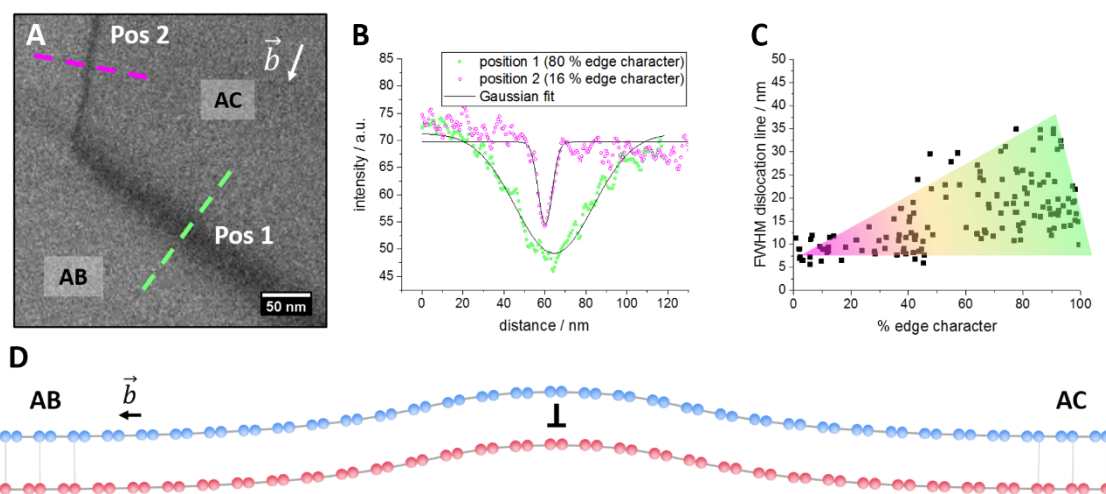surfaces of graphene as seen in the secondary electron image.

Fig. S4. The relationship between dislocation type and line width. Depending on the angle between dislocation line ($\vec{u}$) and Burgers vector ($\vec{b}$) the thickness (or width) of the contrast generated by a dislocation changes drastically. In **A** a tSEM image of a single dislocation with changing character along the dislocation line is shown. While being almost pure edge type at position 1 ($\vec{b} \perp \vec{u}$), the dislocation character at position 2 is changed to predominately screw type (arrow represents the Burgers vector of the dislocation). **B** Intensity profile extracted from indicated positions in **A** demonstrating the increase in contrast broadness for higher edge character. **C** FWHM of Gaussian curves fitted to line scans across a large number of dislocations with different degree of edge character. **D** Schematic of a pure edge partial dislocation $\vec{b} \perp \vec{u}$ in bilayer graphene projected along the dislocation line**.** The edge character leads to an out-of-plane buckling of the membrane resulting in a broadened topographic contrast in tSEM. In reality the buckling is laterally much more extended than depicted in the schematic. The extension of the buckling strongly depends on whether there are other dislocations (or the hole edge of the Quantifoil support) nearby which also affect the layer topography. This explains the increased scattering of dislocation contrast width for increasing edge character (**C**).
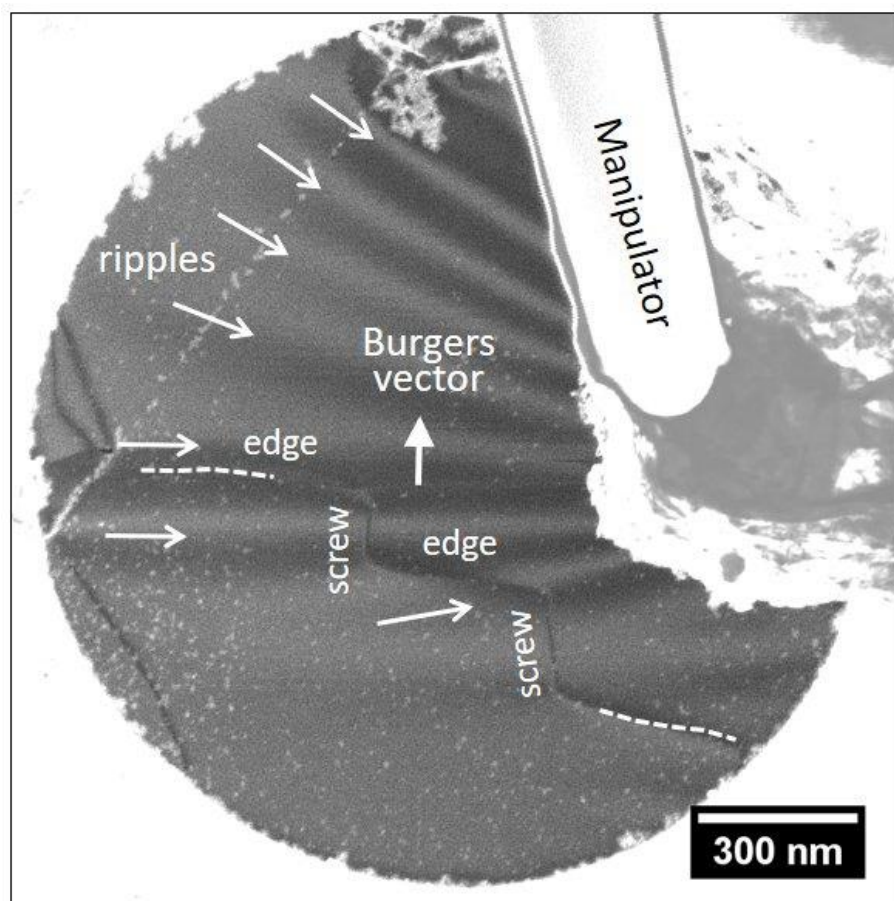
Fig. S5. Example demonstrating the interplay of membrane topography and dislocation line direction. In the present case a pronounced membrane topography is introduced with the help of a micromanipulator. (The dirt on the tip resulted from the mechanical cleaning of the membrane before manipulation.) By pressing the manipulator onto the membrane ripples emerge from the tip of the manipulator (see arrows). An in-plane dislocation (dashed line) running inclined to the ripples shows zigzagging with edge-type and screw-type dislocation segments preferentially aligned parallel and perpendicular to the ripples.
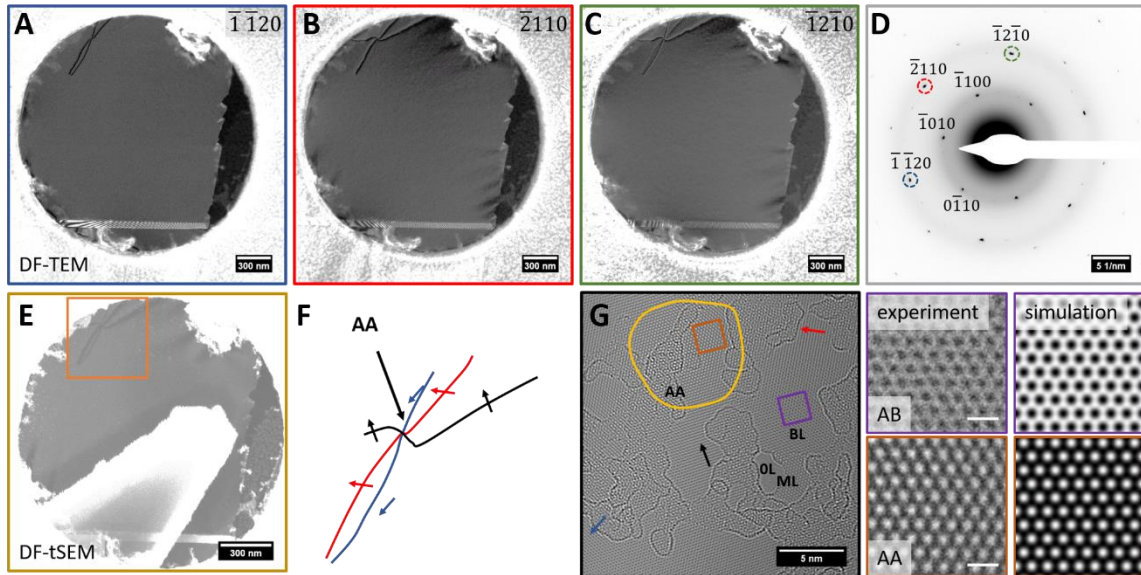
Fig. S6. AA stacking in dislocation nodes. A to **C** DF-TEM images of dislocation network with 3 dislocations of different Burgers vector. DF data acquired based on diffraction spots indicated in **D**. **E** Still frame of manipulation experiment with the same arrangement of dislocations shown in **A** to **C**. **F** Close-up drawing of dislocations within the network. Colored arrows indicate the direction of the respective Burgers vectors. At the crossing point of all 3 dislocations a virtual quantum dot of energetically unfavoured AA stacking is obtained. **G** HRTEM with AA stacking indicated by circle. Arrows represent the dislocations leading towards the AA stacked area. Amorphous residuals are visible as disordered structures. At the lower right 0L indicates a hole, ML a monolayer and BL the bilayer area within the micrograph. At indicated areas close up of AB and AA stacked bilayer graphene alongside a multislice simulation (scale bar is 5 Å). Contrast changes from bright atom contrast (AB-BLG) to dark atom contrast (AA-BLG). Simulation results for 3 nm defocus.
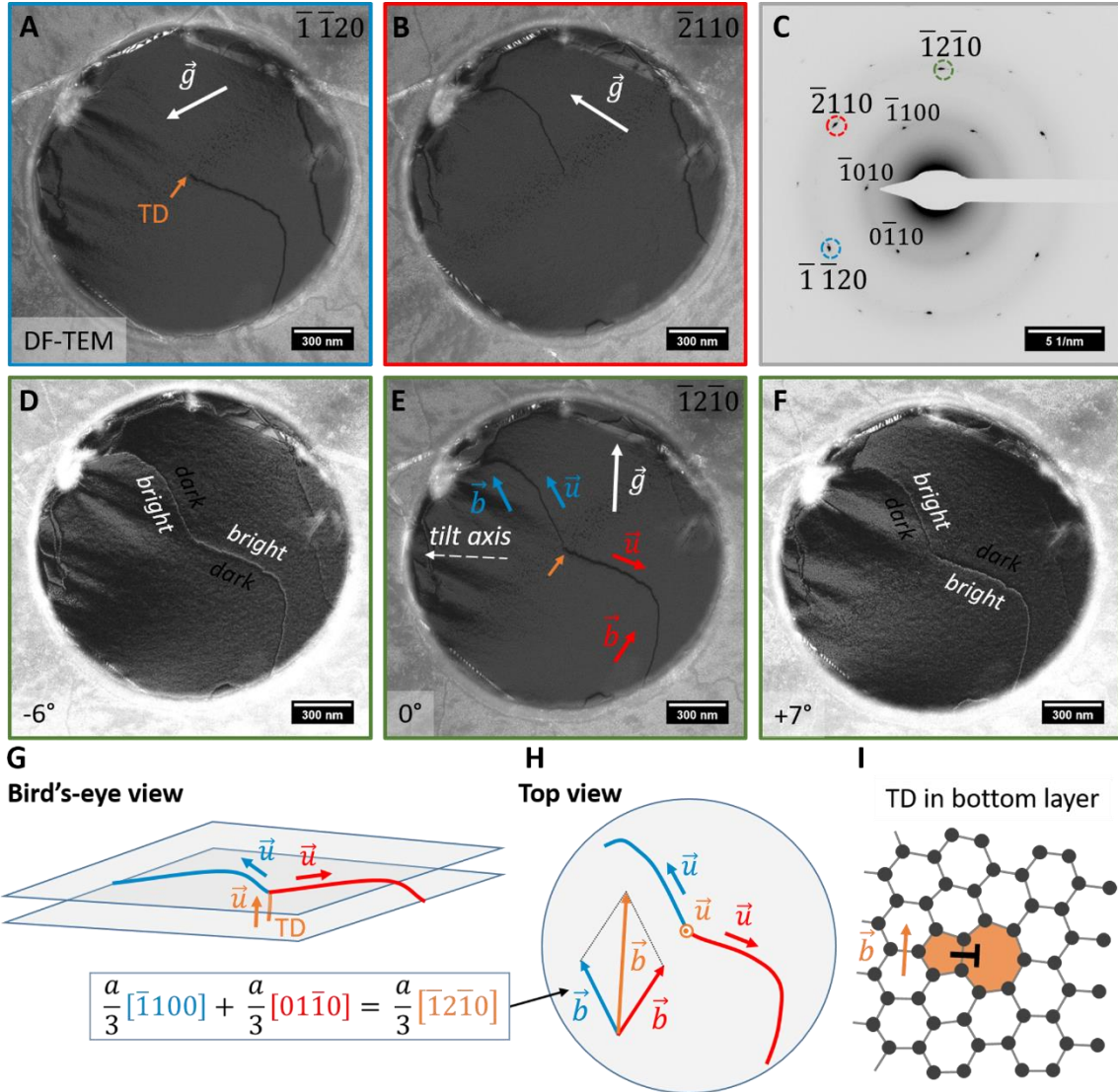
Fig. S7. Complete analysis of the Burgers vector of dislocations. DF-TEM investigation for evaluation of the complete Burgers vectors (including sign) of dislocations meeting at a node introduced by an out-of-plane dislocation (threading dislocation, TD). Two in-plane dislocations with different Burgers vectors are visible in **A** and **B**. From the invisibility criterion ($\vec{g} \cdot \vec{b} = 0$) in **A** and **B** the two dislocations are identified as partial dislocations with Burgers vectors of $\pm \frac{a}{3}[\bar{1}100]$ and $\pm \frac{a}{3}[01\bar{1}0]$, respectively. Both dislocations are pinned to a threading dislocation (TD) as indicated by the orange arrow. Even though the TD is not directly visible its existence results from the fundamental rule of conservation of the total Burgers vector at dislocation nodes *(22)*. Upon tilting the membrane (tilt axis indicated in **E**) the dislocation contrast becomes asymmetric and changes from dark-bright (at -6° tilt, **D**) to bright-dark (at +7° tilt, **F**) for the predominantly edge-type dislocation (red in **E**) and vice versa for the predominantly screw-type dislocation (blue in **E**). This behavior results from the local variation of the excitation error due to lattice plane tilting in the strain field of the dislocations and can be

used to derive the absolute sign of the Burgers vectors. (For the predominately edge-type dislocation lattice strain effectively relaxes by buckling *(10)* which also introduces lattice plane tilting (as schematically depicted in fig. S4 **D**)). **G-H** Schematic bird's eye and top view of dislocation arrangement with arbitrarily defined line vectors. Using these line vectors and the contrast behavior upon tilting the complete Burgers vectors (including sign!) of the two basal dislocations are identified as $\frac{a}{3}\left[\bar{1}100\right]$ and $\frac{a}{3}\left[01\bar{1}0\right]$ using the FS/RH convention for the Burgers vector definition. Most importantly, making use of the rule of conservation of the total Burgers vector at dislocation nodes the threading dislocation is identified as a perfect dislocation in monolayer graphene with a line vector perpendicular to the graphene plane and a Burgers vector of $\frac{a}{3}\left[\bar{1}2\bar{1}0\right]$ as shown in **H**. **I** The perfect dislocation in monolayer graphene can be described by an inserted stripe of atoms (from left) ending in a 5-7-ring in agreement with earlier theoretical *(28)* and experimental *(27)* work. We believe that dislocations of this type (preferentially in a low-angle grain boundary configuration, see Fig. 2 in main manuscript) originate from merging of two slightly misoriented graphene grains/islands during CVD growth.
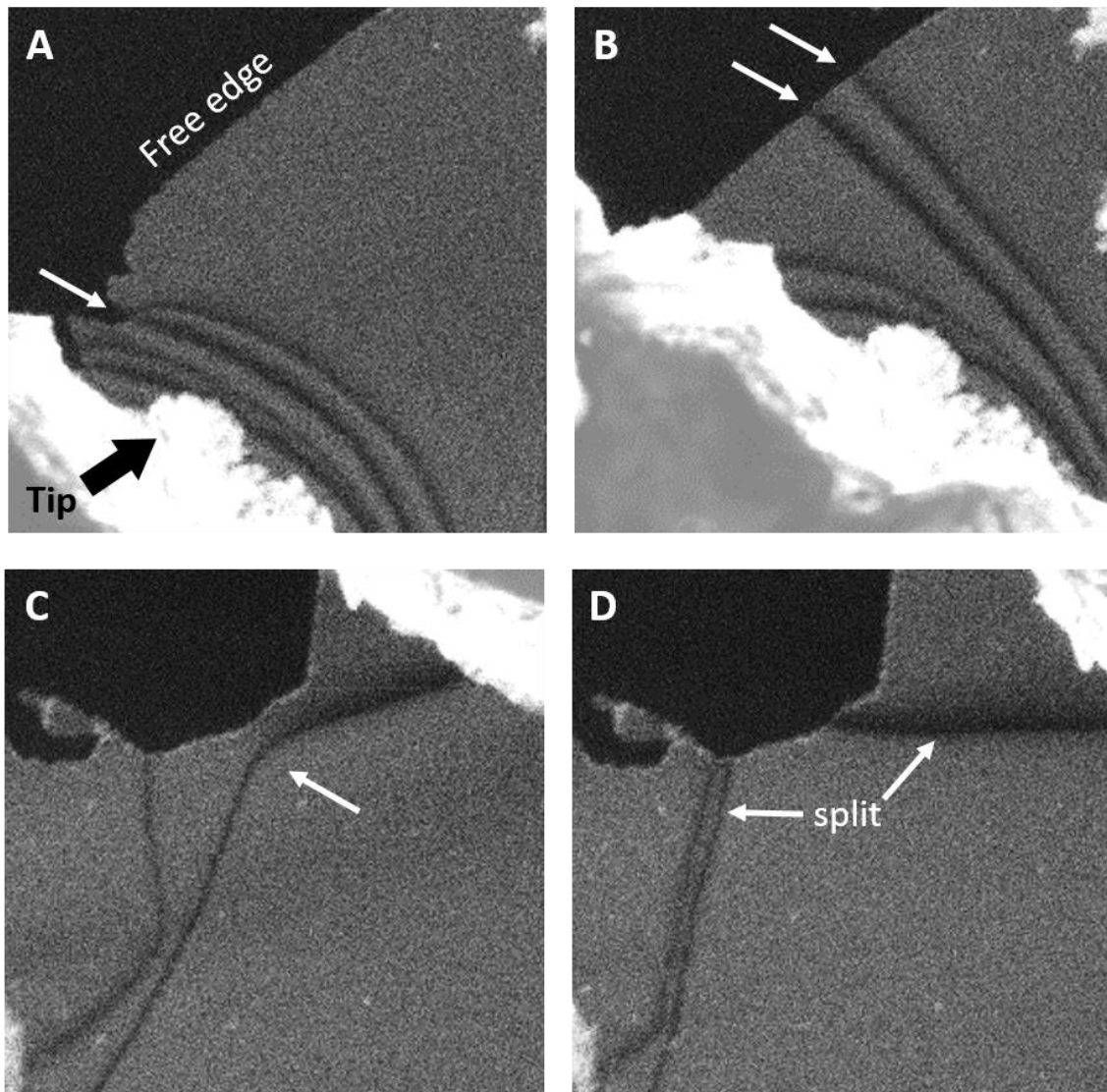
Fig. S8. Dislocation interaction with free edges. A Two dislocations are pinned at a kink in the free edge. The barrier can be overcome by direct manipulation (shown in **B**), after which the dislocations can move freely along the edge. **C** and **D** Dislocation splitting reaction at an edge. Due to the direct manipulation a dislocation interacts with a free edge and splits its line into two parts, both ending at the free edge.

Captions for Supporting Movies

Movie S1. Exemplary cleaning of bilayer graphene. Two manipulators (top and bottom) are dragged over both free surfaces of bilayer graphene suspended over a hole of a Quantifoil film. The amorphous contamination accumulates on the tips (already accumulated contamination from previous experiments is visible) and is pushed from the membrane area towards the support film. After cleaning of the membrane the dislocations are clearly visible.

Movie S2. Manipulation of three individual dislocations showing fundamental properties of dislocations. The length of the dislocation lines can be extended to almost 2 µm while at the upper right part of the membrane a node is formed which contains AA stacking. After retraction of the manipulator tip, the dislocations relax to the initial configuration as a consequence of line tension.

Movie S3. Manipulation of an array of dislocations pinned to threading dislocations. The switching process induced by the manipulator tip can be followed. The switching changes the topology of the system. Contamination re-accumulates during imaging and is visible as bright dots on the surface.

Movie S4. The whole, unabridged manipulation from movie S3. This video includes the second part of the cleaning process. The movie demonstrates the proximity and precision at which the manipulators need to be operated. Additionally, the speed at which electron-beam induced contamination can accumulate is shown.